HHS Public Access

Author manuscript

Eur Radiol. Author manuscript; available in PMC 2016 August 01.

Published in final edited form as:

Eur Radiol. 2016 August ; 26(8): 2547–2558. doi:10.1007/s00330-015-4087-3.

Evaluation of breast cancer using intravoxel incoherent motion (IVIM) histogram analysis: comparison with malignant status, histological subtype, and molecular prognostic factors

Gene Young Cho[1,2], **Linda Moy**[1,2], **Sungheon G. Kim**[1,2], **Steven H. Baete**[1,2], **Melanie Moccaldi**[3], **James S. Babb**[1,2], **Daniel K. Sodickson**[1,2], and **Eric E. Sigmund**[1,2]

[1]Center for Advanced Imaging Innovation and Research (CAI^{2}R), New York University School of Medicine, 660 First Ave. 4th Floor, New York City, NY 10016, USA

[2]Bernard and Irene Schwartz Center for Biomedical Imaging, Department of Radiology, New York University School of Medicine, New York, NY 10016, USA

[3]New York University Langone Medical Center - Cancer Institute, New York, NY 10016, USA

Abstract

Purpose—To examine heterogeneous breast cancer through intravoxel incoherent motion (IVIM) histogram analysis.

Materials and methods—This HIPAA-compliant, IRB-approved retrospective study included 62 patients (age 48.44±11.14 years, 50 malignant lesions and 12 benign) who underwent contrast-enhanced 3 T breast MRI and diffusion-weighted imaging. Apparent diffusion coefficient (ADC) and IVIM biomarkers of tissue diffusivity (D_t), perfusion fraction (f_p), and pseudo-diffusivity (D_p) were calculated using voxel-based analysis for the whole lesion volume. Histogram analysis was performed to quantify tumour heterogeneity. Comparisons were made using Mann–Whitney tests between benign/malignant status, histological subtype, and molecular prognostic factor status while Spearman's rank correlation was used to characterize the association between imaging biomarkers and prognostic factor expression.

Results—The average values of the ADC and IVIM biomarkers, D_t and f_p, showed significant differences between benign and malignant lesions. Additional significant differences were found in the histogram parameters among tumour subtypes and molecular prognostic factor status. IVIM histogram metrics, particularly f_p and D_p, showed significant correlation with hormonal factor expression.

Conclusion—Advanced diffusion imaging biomarkers show relationships with molecular prognostic factors and breast cancer malignancy. This analysis reveals novel diagnostic metrics that may explain some of the observed variability in treatment response among breast cancer patients.

gyc219@nyumc.org.

Keywords

Intravoxel incoherent motion; Breast MR; Diffusion-weighted MRI; Tumour heterogeneity; Breast cancer

Introduction

Heterogeneity is a known hallmark of cancer [1–3], and confounds treatment planning and prevents effective drug delivery. Breast cancer is a prime example in which such heterogeneity can be clearly observed [4].

To quantitatively analyze this heterogeneous tumour microenvironment, an improved understanding of the connections between imaging markers and molecular markers is required. Recent studies have shown that magnetic resonance imaging (MRI) biomarkers such as apparent diffusion coefficient (ADC) correlate with prognostic factors of breast cancer [5–8]. Diffusion-weighted imaging (DWI) characterizes cancerous tissue cellularity [9, 10], particularly in breast cancer [11–15]. Through DWI, biomarkers have been developed that are sensitive to microvascular flow via the intravoxel incoherent motion (IVIM) effect [16]. Using IVIM, first proposed by LeBihan [16], one can quantify tumour hypervascularity and hypercellularity, and these IVIM markers have been shown in a range of studies [17–21], including breast cancer in preclinical [22, 23] and clinical settings [15, 24–28].

However, most studies have focused on average values of IVIM parameters. More information can be parsed from a histogram analysis of the spatial distribution of IVIM parameters [19]. Histogram analysis can provide information beyond the mean values, such as the skewness, and kurtosis of the parameter distributions [22, 29–32]. This additional analysis can potentially provide metrics for additional information on the heterogeneous tumour composition.

In this study, we calculate advanced diffusion MRI metrics from histogram analysis [average, extrema (maximum and minimum), and heterogeneity (kurtosis, skewness, standard deviation [SD])]. While it has been shown in previous studies that IVIM metrics can distinguish between benign and malignant lesions [15, 26, 28], we hypothesize that advanced metrics using histogram analysis can also potentially distinguish between tumour subtypes as well as better differentiate between tumours based on prognostic factors.

Materials and methods

Patients

In this Health Insurance Portability and Accountability Act of 1996 (HIPAA)-compliant, local institutional review board (IRB)-approved retrospective study, 62 patients underwent standard breast MR evaluation for staging of local disease between 1/7/2009 and 2/27/2013. Of these, 50 patients had confirmed malignant lesions and 12 patients had benign lesions (Table 1). Benign lesion classifications included fibrocystic change (n=4), cyst (n=1), atypical ductal hyperplasia (n=1), intraductal papilloma (n=2), fibroadenomas (n=2), and

other benign (n=2). All patients were newly diagnosed breast cancer patients and selected based on having unifocal disease. The mean age of all patients was 48.4±11.1 years (malignant lesion: 50.2±10.5 years; benign lesion: 46.3±11.7 years) with a range of 25–80 years. Patients were diagnosed with breast cancer either through stereotactic core biopsy, ultrasound (US)-guided fine needle aspirations (FNA), or MRI-guided core biopsy. Final histopathology diagnosis was confirmed through histology, surgery, and clinical follow-up. No new malignancies were found in either group within the follow-up periods (average 2.6 years; range: 1 month to 4.8 years). One patient, however, received treatment elsewhere after initial examinations; no follow-up results were recorded.

MRI scans

Patients underwent a bilateral MRI breast examination in a full body Siemens Tim Trio 3 T MRI scanner (Siemens Medical Solutions, Erlangen, Germany) using a seven-element breast coil array (Invivo Corp., Gainesville, FL, USA). Anatomical imaging was performed using a T1-weighted, volume-interpolated breath hold examination (VIBE) sequence with and without fat saturation [saturation time/echo time (TR/TE)=3.66/1.1 ms, matrix 384×384, 288 slices, resolution 1.2×0.9×1.5 mm^3 and scan time 1:10 each]. Total scan time was 2.3 min.

DWI protocol was collected using a twice refocused, bipolar gradient single-shot centric-ordered turbo-spin echo (TSE) sequence (TR/TE=2000/103 ms, 108*×128 matrix, 12 axial slices, 2.7×2.7×4.0 mm voxel, parallel imaging [generalized auto-calibrating partially parallel acquisition (GRAPPA)] acceleration factor (iPat)=2, 24 reference lines; *Note: 8 patients used a phase matrix of 128 rather than 108). Axial TSE–DWI images with bilateral breast coverage were collected with frequency-selective fat suppression and diffusion sensitization in the anterior–posterior direction applied with weighting factors (b-values) of 0, 30, 70, 100, 150, 200, 300, 400, 500, 800 s/mm^2 (total scan time=4 minutes). A TSE diffusion-weighted (DW) sequence was used instead of echo planar imaging to avoid susceptibility artifacts [33, 34]. The slices measured in the TSE–DWI scan covered the lesion as identified in the anatomical scan. A fat-saturated sagittal T2-weighted TSE scan (TR/TE=6070/84 ms, matrix 384 × 336, 88 slices, iPat = 2, resolution 1.0 × 1.0 × 5.0 mm^3) was performed pre-contrast for a total scan time of 4.5 min. Patients also underwent dynamic contrast-enhanced (DCE) MRI. Contrast-enhanced scans consisted of three-dimensional (3D), T1-weighted, sagittal fat-saturated VIBE images (TR/TE=4.23/1.55 ms, matrix 384 × 336, 224 slices, iPat = 2, resolution 0.7 × 0.7 × 1.5 mm^3) and collected one pre-contrast and 4 consecutive time points after administration of gadolinium (Gd–DTPA) contrast agent (Magnevist, dosage 0.1 mM/kg body weight; average 14.6±5.1 cc). Scan duration was 1:13 for each, and total scan time lasted around 6 minutes. An axial 3D VIBE scan was collected post-contrast (TR/TE=4.23/1.55 ms, matrix 384×384, 224 slices, resolution 1.3×1.1×1.5 mm^3) with a total scan time of 2.5 min. The images from this scan were used for guidance of region of interest (ROI) selection during analysis of the DW images. IVIM and contrast-enhanced data from 36 (out of 62) subjects were previously reported [25, 27], but without parametric map analysis or comparison with molecular prognostic factors.

Data analysis

The image processing workflow for this study is illustrated in Fig. 1. Two breast radiologists with over 5 years of experience independently identified lesions on anatomical images based on the hyperintense signals from post-contrast axial and sagittal T1 VIBE images. Lesion characteristics were recorded according to the American College of Radiology breast imaging-reporting and data system (ACR BI-RADS) MR lexicon [35]. The lesions were located in the TSE-DWI images using methods similar to previous studies [11, 27, 36]. Quantitative DWI analysis was performed with custom code (Igor Pro 6, WaveMetrics, Inc., Portland, OR, USA). Images were first analyzed voxel-by-voxel using a mono-exponential decay model with all b-values to produce ADC maps for all slices:

$$M/M_0 = e^{-b \cdot ADC} \quad (1)$$

Here, M is the DW magnetization and M_0 is the total reference magnetization. ADC maps, weighted and unweighted diffusion images, and post-contrast VIBE images guided lesion segmentation. An ROI was drawn by a single operator (based on consensus of the two breast radiologists) on the whole lesion volume for each slice, excluding normal fibroglandular tissue (FGT) and adipose tissue.

IVIM analysis

Bi-exponential analysis is used to quantify biomarkers of the IVIM model [16]. The signal decay curve as a function of increasing b-value is fitted to a bi-exponential equation:

$$M/M_0 = f_p \cdot e^{-b \cdot D_p} + (1 - f_p) \cdot e^{-b \cdot D_t} \quad (2)$$

where f_p is perfusion fraction, D_p is pseudo-diffusivity, and D_t is tissue diffusivity. For all analyses, a "segmented" approach was employed to extract the IVIM parameters [17, 37–43]. The first step is to fit all b-values>200 s/mm^2 data mono-exponentially to obtain D_t, on the assumption that the pseudo-diffusion is negligible in this regime, and then extrapolate the mono-exponential fit to b=0 to estimate f_p. The second step is to constrain D_t and f_p in the bi-exponential fit for Eq. (2) to obtain D_p.

Parametric maps and voxel-based analysis for IVIM parameters (D_t, f_p, and D_p) were derived within the tumour ROI described above. Within the voxel-based analysis, an additional filter was generated to only select voxels of highly vascular tumour tissue (VTT) [44]. Specifically, the residuals of the mono-exponential and bi-exponential fit from Eqs. (1) and (2), respectively, were used to calculate the Bayesian information criterion (BIC); the fit (mono-exponential or bi-exponential) with the lower BIC value is validated for that voxel. A vascular tumour tissue (VTT) mask was then generated from all voxels with (a) lower bi-exponential than mono-exponential BIC and (b) ADC<2 μm^2/ms to exclude necrotic or normal tissue regions. This VTT filter was used to compute the percentage of VTT voxels from total voxels analyzed in each lesion (labelled as VTT%).

Histogram analysis

Histogram analysis was performed to extract mean, extrema, and heterogeneity metrics. Following manual lesion segmentation, histograms were generated from each parameter using the following standardized parameter ranges: 0.01 $\mu m^2/ms$<ADC, 0.01<D_t<3 $\mu m^2/ms$; 0.01<D_p<100 $\mu m^2/ms$; 0<f_p<100 %. Voxels for which fits generated unphysical values (<0) were nulled (set to zero) for outlier rejection. Percentages of excluded voxels outside these ranges were computed for each parameter. Maximum and minimum values were extracted from the distribution. Given the outlier rejection scheme, the minimum value f_p was often zero; and given its equal value amongst all lesions, the f_p minimum was excluded from statistical analysis. Higher order moment calculations were performed in a standard method [19, 22, 29–32] to compute SDs, kurtosis, and skewness values from each lesion's histogram and its distribution.

Histopathological data analysis

Immunohistochemistry data were collected from 45 out of the 50 patients with malignancies (Table 1), who underwent an imaging-guided biopsy. In addition, not all histological data was available for each patient, as indicated in Table 1 (e.g. hormonal tests were available for a given patient, but not Her2/neu). Histological subtype was determined for all lesions. Using percentage expression of molecular prognostic factors, positive expression for hormonal receptors [HR; specifically, oestrogen receptor (ER) and progesterone receptor (PR)] were defined as ≥10 %; for cellular proliferation stain Ki-67 also ≥10 %; and for Her2/neu expression, scores higher than +1 [45]. Table 1 shows the number of patients for which prognostic factor data was available. Treatment paradigm categories were defined based on recent consensus [46]: ER-positive and Her2-negative (ER+HER2−), ER-positive and Her2-positive (ER+HER2+), ER-negative and Her2-positive (ER-HER2+), and ER-negative and Her2-negative (ER-HER2− or TN).

Statistical analysis

Each subject contributed to exactly one value of each imaging measure to the analyses. Exact Mann–Whitney (MW) tests were used to compare subject groups defined in terms of tumour type (benign versus malignant), histological subtype, or marker status (positive versus negative) with respect to each imaging measure. Kruskal–Wallis tests were used to compare subject groups that had more than two groupings. We also used MW tests to compare IVIM parameters between groups defined by treatment paradigms (ER+HER2−, ER+HER2+, ER-HER2+, and TN). Due to our small sample size, we limited analyses to comparing a specific group to all others, e.g. TN (n=15) versus all other patients. The Spearman rank correlation was used to characterize the correlation of imaging measures with expression level of each marker. Binary logistic regression and region of concern (ROC) analyses were used to assess the diagnostic utility of the imaging measures, alone and in combination, for the detection of malignant lesions or lesions characterized as positive for a given marker or constellation of markers. The area under the ROC curve (AUC) and *p* values from logistic regression were used to assess the diagnostic utility of each imaging measure for the detection of lesions characterized as positive for a given constellation of markers. Sensitivity, specificity, and overall accuracy were computed at the

threshold value of each numeric measure that maximized the Youden index in an ROC analysis. All statistical tests were conducted at the two-sided 5 % significance level using SAS 9.3 (SAS Institute, Cary, NC).

Results

MRI data

From the total number of malignant lesions (n=50), 35 masses and 15 non-mass enhancements were identified. The mean size of the largest axis of malignant lesions from histopathology data was 3.25±2.72 cm (range 1.2 to 12.7 cm) and that from MR contrast-enhanced data was 3.69±2.71 cm (range 1.2 to 12.9 cm). Average total ROI size for the whole lesion on DWI was 15.38 cm^3 (range 0.28 to 164.16 cm^3) for breast cancer patients and 1.84 cm^3 (range 0.28 to 3.57 cm^3) for benign cases. The percentage of excluded voxels represented a minority fraction for all parameters (D_t: 9.19±16.81 %; f_p: 5.67±9.85 %; D_p: 17.61±34.02 %). Figure 2 shows parametric map results from three patients with different tumour subtypes: (i) DCIS (Fig. 2a–e), (ii) invasive lobular carcinoma (Fig. 2f–j), and (iii) invasive ductal carcinoma (Fig. 2k–o). The histogram results for the patient with invasive ductal carcinoma are shown below each of the patient's parameter maps.

Benign versus malignant

Using MW tests, average ADC values were significantly lower for patients with malignant lesions (p=0.040; Fig. 3a). These patients also had significantly lower D_t (p=0.003) and higher f_p (p=0.019) than those with benign lesions (Fig. 3b–c). Histogram analysis also revealed other significant differentiators between benign and malignant with a majority of these findings coming from extrema or heterogeneity markers of f_p or D_p with two examples (maximum f_p and D_p kurtosis) shown in Fig. 3d and e. VTT% was also found to be significantly different between benign and malignant groups (p=0.040; Fig. 3f).

The ROC analyses to assess diagnostic utility for the detection of malignant lesions (Table 2) reveals that the average D_t and f_p values had higher AUC values (0.77 and 0.72, respectively) and accuracy percentages (71.0 % and 72.6 %, respectively) than ADC (AUC=0.69, accuracy=62.9 %). Regarding parameter combinations, malignancy was independently predicted by the combination of minimum D_t (p=0.004), D_p skewness (p = 0.017), D_t skewness (p = 0.036), and minimum ADC (p=0.011), which together achieved an AUC of 0.917.

Subtype comparison

Using MW tests, significant differences among tumour subtypes were only found when comparing ADC and D_t metrics (Tables 3 and 4). Average ADC and D_t values were significantly lower in the invasive or mixed groups than in the DCIS groups (Table 3). Comparisons of IVIM histogram parameters between lesions of histological subtypes showed all but one of the significant differences (maximum f_p) came from extrema or heterogeneity parameters of ADC and D_t (Table 4). Results from a Kruskal–Wallis test also indicated significance for comparing subtypes for average and histogram parameters of ADC and D_t.

Molecular prognostic factor comparisons and correlations

As shown in Table 5 and Fig. 4, when using MW tests, many significant differences among groups defined by hormonal status involved the heterogeneity metrics from f_p and D_p. The heterogeneity metrics of the vascular-based IVIM parameters showed significant differences between groups with hormonal positive and negative status (Fig. 4a–b). In addition, f_p and D_p heterogeneity metrics also differentiated between Ki-67-positive and Ki-67-negative status (Fig. 4c), and average D_p values significantly differentiated Her2/Neu status (Fig. 4d).

Regarding Spearman correlations of IVIM parameters with expression levels of prognostic factors, significant correlations were mostly observed between hormonal expression (ER, PR) and vascular parameters (f_p, D_p), largely involving the heterogeneity metrics (kurtosis and skewness). Figure 5 shows the significant correlation coefficients (R) connecting imaging parameters and prognostic factors. When including all parameters, a total of 18 different correlations out of a possible 92 (~20 %) were significant between IVIM parameters and the molecular prognostic factors (Fig. 5). Of these, 12 heterogeneity metrics showed an average R of 0.40, 5 extrema values showed an average R of 0.41, and 1 average value from f_p (%) showed an R of 0.33.

Table 6a shows the IVIM histogram parameters showing significant differentiation of lesion subtype groupings (ER+HER2−, ER+HER2+, and TN) by either MW group comparison or logistic regression. D_p showed the most significant differentiators for the IVIM histogram parameters. For ER+HER2− and ER+HER2+ groups, D_p average, skewness, and kurtosis values were significant differentiators, with ADC average also differentiating the ER +HER2+ group. Similarly, for the TN group, maximum D_p and f_p skewness showed significant differentiation by MW testing.

Table 6b shows the results from analyses to identify combinations of metrics that independently predict prognostic factor status (e.g. discriminate ER+ from ER−) or group membership defined by multiple prognostic factors (e.g. TN cancers). There was no set of two or more measures that were independent predictors of ER only, Her2/Neu only, Ki67, hybrid, or TN status. Cases with at least one hormonal positive expression were independently predicted by the set of measures D_t standard deviation, f_p kurtosis, and D_p skewness; or ADC standard deviation, f_p skewness, and D_p skewness. PR positivity was independently predicted by the set of measures D_t standard deviation, f_p kurtosis, and D_p skewness as well as f_p skewness and D_p skewness. Finally, ER+HER2− patients were independently predicted by the combination of D_p average and D_p skewness.

Discussion

This study illustrates the spatial heterogeneity found in cellularity and angiogenesis through IVIM biomarkers. Histogram analysis helps distinguish between tumour subtypes and reveals correlations with prognostic factors. In combination with guidance from contrast-enhanced imaging, the image quality of the TSE-DWI results collected was sufficient to delineate and segment each lesion for whole-volume histogram analysis.

Recent studies of IVIM in breast cancer [15, 26–28], demonstrated that f_p significantly differentiates malignant from benign lesions, as shown in the present study. Malignant lesions are more cellular and vascular than benign entities; the IVIM approach can separate these effects to avoid conflicting contrast. The results from the ROC analysis show that significant malignant/benign differentiation was provided via both D_t and f_p, with stronger accuracy than with ADC alone.

IVIM analysis also shows significant differences between different tumour subtypes. Invasive breast and lung cancers (IDCs and ILCs, respectively) displayed lower ADC and D_t values. These are more aggressive cancers, with generally higher cell density. In addition, IVIM histogram analysis may have the ability to potentially separate the heterogeneous mixed tumour type, which contains both DCIS and invasive cancer cells. Likewise, histogram analysis has merits when comparing between molecular prognostic factors. This correlation with prognostic factors evidently involves both the magnitude and the spatial distribution of blood volume.

Several studies have considered the relationship of ADC with prognostic factors in breast cancer [5, 8, 14]. A key finding in these reports is a significantly lower ADC value in ER+ tumours, which is speculated to be related to a lower perfusion contribution. While relationships between ER status and vascularity are not uniform [47, 48], the present study seems to confirm that the ADC versus ER findings in human breast tumours are indeed vascular, based on the significantly lower D_p kurtosis and skewness in ER+ tumours and the significant negative correlations between f_p kurtosis and skewness and D_p kurtosis and skewness with ER expression. Interestingly, mean f_p values correlated positively with PR expression. Similarities in hormone receptor effects would suggest a negative correlation, as with ER expression; however, PR+ expression tumours may increase tumour growth by angiogenesis through the normalization of tumour vasculature, which would allow for proper blood flow. In fact, studies have shown that progesterone may increase angiogenesis through regulation of VEGF in breast cancer cells [49]. Moreover, tamoxifen treatment has been shown to be more effective in patients with higher PR+ expression [50]. However, a more extensive observation of this relationship is needed to confirm these findings.

ER expression showed the most significant correlations with the diffusion parameters (Fig. 5). This may indicate the potential to provide a surrogate measure of ER expression through noninvasive imaging tools. Within the IVIM parameter set, the biggest contributing predictive factors were f_p and D_p, and IVIM parameters showed more significant correlations with prognostic factors than ADC alone. IVIM analysis, therefore, appears to provide a more nuanced representation of the microenvironment, with connection to hormonal expression levels. A combination analysis using the most promising parameters showed improvement in accuracy in discriminating between different prognostic factors or treatment paradigms. It is noteworthy that several such predictive sets involved heterogeneity metrics of all three IVIM parameters, showing the benefit of extending beyond both the ADC parameter and mean value descriptions.

This study was limited by a relatively small sample size and did not employ multiple comparison corrections. The tumour segmentation workflow was performed by a single

reader who was not blinded to malignancy status. Neither age nor menstrual cycle were controlled for in the enrolment. Also, the bi-exponential IVIM fitting model can be problematic, with the estimation of vascular diffusion effects at lower b-values (b<200 s/mm^2) being most challenging. A variety of methods have been employed to address this challenging quantification; fitting methods including optimized sampling patterns [25, 51, 52], fitting algorithms [24, 53–57], or fit models [58, 59] can improve the precision of IVIM parameters. Others have also employed maximum likelihood (ML) estimation [60, 61] or used “fusion bootstrap moves” [62]. The segmented approach taken in the current study was adopted as a compromise between precision, accuracy, and practicality; future studies may invoke more advanced strategies. Additionally, the standardized parameter ranges for histogram calculation excluded differing lesion fractions for each parameter (such as from fit non-convergence, failure of the fit algorithm approximation, or macroscopic flow effects) and may have induced biases.

Heterogeneity could also exist in tumour subtype and prognostic factor expression. Classification schemes based on biopsy sampling can be approximate representations of the tumour aggressiveness. Thus, while the imaging/prognostic factor correlations observed here increase experimental understanding of tumour biology, imaging surrogates of the molecular prognostic factors need not be the only predictive route. Rather, the prognostic value of the IVIM biomarkers should be evaluated in longitudinal breast cancer treatment studies.

Understanding the full lesion characterization through imaging biomarkers and observing their utility in treatment monitoring for neoadjuvant therapies can vastly change the clinical landscape. This not only lessens the need for invasive biopsy procedures, but it can also give clinicians abilities to strategize the timing of drug deliveries as they quickly interpret the patient’s response to treatment. The prediction of treatment response in the neoadjuvant setting is a significant opportunity to apply quantitative imaging to breast cancer; studies have been performed using either ADC, DCE biomarkers, or both (see meta-analyses: [63, 64]). Future studies will explore whether the combination of advanced IVIM modelling and spatial histogram analysis can advance predictive ability in the neoadjuvant setting. This study suggests that a comprehensive evaluation of breast cancer patients using advanced imaging may increase insight into tumour physiology, and potentially contribute to individualized treatment plans for high-risk women.

Acknowledgments

The scientific guarantor of this publication is Eric E. Sigmund, Ph.D. The authors of this manuscript declare no relationships with any companies whose products or services may be related to the subject matter of the article. The authors state that this work has not received any funding. One of the authors has significant statistical expertise (James S. Babb). Institutional review board approval was obtained. Written informed consent was waived by the institutional review board. Some study subjects or cohorts have been previously reported in

- Sigmund EE, Cho GY, Kim S et al (2011) Intravoxel incoherent motion imaging of tumour microenvironment in locally advanced breast cancer. Magn Reson Med 65:1437–1447
- Cho GY, Moy L, Kim SG, Klautau Leite AP, Baete SH, Babb JS, Sodickson DK, Sigmund EE (2015) Comparison of contrast enhancement and diffusion-weighted magnetic resonance imaging in healthy and cancerous breast tissue. Eur J Radiol 84(10):1888–93. doi: 10.1016/j.ejrad.2015.06.023. Epub 2015 Jul 2.

- Cho GY, Moy L, Zhang JL et al (2014) Comparison of fitting methods and b-value sampling strategies for intravoxel incoherent motion in breast cancer. Magn Reson Med. 10.1002/mrm.25484

Methodology: retrospective, diagnostic or prognostic study, performed at one institution.

References

1. Meacham CE, Morrison SJ. Tumour heterogeneity and cancer cell plasticity. Nature. 2013; 501:328–337. [PubMed: 24048065]
2. Durrett R, Foo J, Leder K, Mayberry J, Michor F. Intratumor heterogeneity in evolutionary models of tumor progression. Genetics. 2011; 188:461–477. [PubMed: 21406679]
3. Fisher R, Pusztai L, Swanton C. Cancer heterogeneity: implications for targeted therapeutics. Br J Cancer. 2013; 108:479–485. [PubMed: 23299535]
4. Polyak K. Heterogeneity in breast cancer. J Clin Invest. 2011; 121:3786–3788. [PubMed: 21965334]
5. Jeh SK, Kim SH, Kim HS, et al. Correlation of the apparent diffusion coefficient value and dynamic magnetic resonance imaging findings with prognostic factors in invasive ductal carcinoma. J Magn Reson Imaging. 2011; 33:102–109. [PubMed: 21182127]
6. Choi SY, Chang YW, Park HJ, Kim HJ, Hong SS, Seo DY. Correlation of the apparent diffusion coefficiency values on diffusion-weighted imaging with prognostic factors for breast cancer. Br J Radiol. 2012; 85:e474–e479. [PubMed: 22128125]
7. Iima M, Le Bihan D, Okumura R, et al. Apparent diffusion coefficient as an MR imaging biomarker of low-risk ductal carcinoma in situ: a pilot study. Radiology. 2011; 260:364–372. [PubMed: 21633054]
8. Kamitani T, Matsuo Y, Yabuuchi H, et al. Correlations between apparent diffusion coefficient values and prognostic factors of breast cancer. Magn Reson Med Sci MRMS Off J Jpn Soc Magn Reson Med. 2013; 12:193–199.
9. Basser PJ. Inferring microstructural features and the physiological state of tissues from diffusion-weighted images. NMR Biomed. 1995; 8:333–344. [PubMed: 8739270]
10. Padhani AR, Liu G, Koh DM, et al. Diffusion-weighted magnetic resonance imaging as a cancer biomarker: consensus and recommendations. Neoplasia. 2009; 11:102–125. [PubMed: 19186405]
11. Sinha S, Lucas-Quesada FA, Sinha U, DeBruhl N, Bassett LW. In vivo diffusion-weighted MRI of the breast: potential for lesion characterization. J Magn Reson Imaging. 2002; 15:693–704. [PubMed: 12112520]
12. Rahbar H, Partridge SC, Demartini WB, et al. In vivo assessment of ductal carcinoma in situ grade: a model incorporating dynamic contrast-enhanced and diffusion-weighted breast MR imaging parameters. Radiology. 2012; 263:374–382. [PubMed: 22517955]
13. Partridge SC, Rahbar H, Murthy R, et al. Improved diagnostic accuracy of breast MRI through combined apparent diffusion coefficients and dynamic contrast-enhanced kinetics. Magn Reson Med. 2011; 65:1759–1767. [PubMed: 21254208]
14. Kim SH, Cha ES, Kim HS, et al. Diffusion-weighted imaging of breast cancer: correlation of the apparent diffusion coefficient value with prognostic factors. J Magn Reson Imaging. 2009; 30:615–620. [PubMed: 19711411]
15. Iima M, Yano K, Kataoka M, et al. Quantitative non-gaussian diffusion and intravoxel incoherent motion magnetic resonance imaging: differentiation of malignant and benign breast lesions. Investig Radiol. 2015; 50:205–211. [PubMed: 25260092]
16. Le Bihan D, Breton E, Lallemand D, Aubin ML, Vignaud J, Laval-Jeantet M. Separation of diffusion and perfusion in intravoxel incoherent motion MR imaging. Radiology. 1988; 168:497–505. [PubMed: 3393671]
17. Luciani A, Vignaud A, Cavet M, et al. Liver cirrhosis: intravoxel incoherent motion MR imaging-pilot study. Radiology. 2008; 249:891–899. [PubMed: 19011186]
18. Lemke A, Laun FB, Klauss M, et al. Differentiation of pancreas carcinoma from healthy pancreatic tissue using multiple b-values: comparison of apparent diffusion coefficient and intravoxel incoherent motion derived parameters. Investig Radiol. 2009; 44:769–775. [PubMed: 19838121]

19. Gaing B, Sigmund EE, Huang WC, et al. Subtype differentiation of renal tumors using voxel-based histogram analysis of intravoxel incoherent motion parameters. Investig Radiol. 2015; 50:144–152. [PubMed: 25387050]
20. Lu Y, Jansen JF, Mazaheri Y, Stambuk HE, Koutcher JA, Shukla-Dave A. Extension of the intravoxel incoherent motion model to non-gaussian diffusion in head and neck cancer. J Magn Reson Imaging. 2012; 36:1088–1096. [PubMed: 22826198]
21. Thoeny HC, Zumstein D, Simon-Zoula S, et al. Functional evaluation of transplanted kidneys with diffusion-weighted and BOLD MR imaging: initial experience. Radiology. 2006; 241:812–821. [PubMed: 17114628]
22. Song YS, Park CM, Lee SM, et al. Reproducibility of histogram and texture parameters derived from intravoxel incoherent motion diffusion-weighted MRI of FN13762 rat breast Carcinomas. Anticancer Res. 2014; 34:2135–2144. [PubMed: 24778015]
23. Kim S, Decarlo L, Cho GY, et al. Interstitial fluid pressure correlates with intravoxel incoherent motion imaging metrics in a mouse mammary carcinoma model. NMR Biomed. 2012; 25:787–794. [PubMed: 22072561]
24. Suo S, Lin N, Wang H, et al. Intravoxel incoherent motion diffusion-weighted MR imaging of breast cancer at 3.0 tesla: comparison of different curve-fitting methods. J Magn Reson Imaging. 2014 doi:10.1002/jmri.24799:n/a-n/a.
25. Cho GY, Moy L, Zhang JL, et al. Comparison of fitting methods and b-value sampling strategies for intravoxel incoherent motion in breast cancer. Magn Reson Med. 2014 doi:10.1002/mrm.25484.
26. Bokacheva L, Kaplan JB, Giri DD, et al. Intravoxel incoherent motion diffusion-weighted MRI at 3.0 T differentiates malignant breast lesions from benign lesions and breast parenchyma. J Magn Reson Imaging. 2014; 40:813–823. [PubMed: 24273096]
27. Sigmund EE, Cho GY, Kim S, et al. Intravoxel incoherent motion imaging of tumor microenvironment in locally advanced breast cancer. Magn Reson Med. 2011; 65:1437–1447. [PubMed: 21287591]
28. Liu C, Liang C, Liu Z, Zhang S, Huang B. Intravoxel incoherent motion (IVIM) in evaluation of breast lesions: comparison with conventional DWI. Eur J Radiol. 2013; 82:e782–e789. [PubMed: 24034833]
29. Wiederer J, Pazahr S, Leo C, Nanz D, Boss A. Quantitative breast MRI: 2D histogram analysis of diffusion tensor parameters in normal tissue. MAGMA. 2014; 27:185–193. [PubMed: 23999995]
30. Chandarana H, Rosenkrantz AB, Mussi TC, et al. Histogram analysis of whole-lesion enhancement in differentiating clear cell from papillary subtype of renal cell cancer. Radiology. 2012; 265:790–798. [PubMed: 23175544]
31. Lutz K, Wiestler B, Graf M, et al. Infiltrative patterns of glioblastoma: identification of tumor progress using apparent diffusion coefficient histograms. J Magn Reson Imaging. 2014; 39:1096–1103. [PubMed: 24115401]
32. Emblem KE, Scheie D, Due-Tonnessen P, et al. Histogram analysis of MR imaging–derived cerebral blood volume maps: combined glioma grading and identification of low-grade oligodendroglial subtypes. Am J Neuroradiol. 2008; 29:1664–1670. [PubMed: 18583405]
33. Baltzer PA, Renz DM, Herrmann KH, et al. Diffusion-weighted imaging (DWI) in MR mammography (MRM): clinical comparison of echo planar imaging (EPI) and half-Fourier single-shot turbo spin echo (HASTE) diffusion techniques. Eur Radiol. 2009; 19:1612–1620. [PubMed: 19288109]
34. Kinoshita T, Yashiro N, Ihara N, Funatu H, Fukuma E, Narita M. Diffusion-weighted half-Fourier single-shot turbo spin echo imaging in breast tumors: differentiation of invasive ductal carcinoma from fibroadenoma. J Comput Assist Tomogr. 2002; 26:1042–1046. [PubMed: 12488758]
35. ACR. Breast imaging reporting and data system (BI-RADS). American College of Radiology; Reston, VA: 2003.
36. Sharma U, Danishad KKA, Seenu V, Jagannathan NR. Longitudinal study of the assessment by MRI and diffusion-weighted imaging of tumor response in patients with locally advanced breast cancer undergoing neoadjuvant chemotherapy. NMR Biomed. 2009; 22:104–113. [PubMed: 18384182]

37. Wirestam R, Borg M, Brockstedt S, Lindgren A, Holtas S, Stahlberg F. Perfusion-related parameters in intravoxel incoherent motion MR imaging compared with CBV and CBF measured by dynamic susceptibility-contrast MR technique. Acta Radiol. 2001; 42:123–128. [PubMed: 11281143]
38. Moteki T, Horikoshi H. Evaluation of hepatic lesions and hepatic parenchyma using diffusion-weighted echo-planar MR with three values of gradient b-factor. J Magn Reson Imaging. 2006; 24:637–645. [PubMed: 16888790]
39. Callot V, Bennett E, Decking UK, Balaban RS, Wen H. In vivo study of microcirculation in canine myocardium using the IVIM method. Magn Reson Med. 2003; 50:531–540. [PubMed: 12939761]
40. Yao L, Sinha U. Imaging the microcirculatory proton fraction of muscle with diffusion-weighted echo-planar imaging. Acad Radiol. 2000; 7:27–32. [PubMed: 10645455]
41. Pekar J, Moonen CT, van Zijl PC. On the precision of diffusion/perfusion imaging by gradient sensitization. Magn Reson Med. 1992; 23:122–129. [PubMed: 1734174]
42. Guiu B, Petit JM, Capitan V, et al. Intravoxel incoherent motion diffusion–weighted Imaging in nonalcoholic fatty liver disease: a 3.0–T MR study. Radiology. 2012; 265:96–103. [PubMed: 22843768]
43. Sumi M, Nakamura T. Head and neck tumors: assessment of perfusion–related parameters and diffusion coefficients based on the intravoxel incoherent motion model. AJNR Am J Neuroradiol. 2013; 34:410–416. [PubMed: 22859281]
44. Schwarz G. Estimating dimension of a model. Ann Stat. 1978; 6:461–464.
45. Adams S, Chakravarthy AB, Donach M, et al. Preoperative concurrent paclitaxel-radiation in locally advanced breast cancer: pathologic response correlates with five-year overall survival. Breast Cancer Res Treat. 2010; 124:723–732. [PubMed: 20878462]
46. Prat A, Perou CM. Deconstructing the molecular portraits of breast cancer. Mol Oncol. 2011; 5:5–23. [PubMed: 21147047]
47. Yue W, Wang JP, Li Y, et al. Tamoxifen versus aromatase inhibitors for breast cancer prevention. Clin Cancer Res. 2005; 11:925s–930s. [PubMed: 15701888]
48. Pequeux C, Raymond-Letron I, Blacher S, et al. Stromal estrogen receptor-alpha promotes tumor growth by normalizing an increased angiogenesis. Cancer Res. 2012; 72:3010–3019. [PubMed: 22523036]
49. Hyder SM, Murthy L, Stancel GM. Progestin regulation of vascular endothelial growth factor in human breast cancer cells. Cancer Res. 1998; 58:392–395. [PubMed: 9458078]
50. Stendahl M, Ryden L, Nordenskjold B, Jonsson PE, Landberg G, Jirstrom K. High progesterone receptor expression correlates to the effect of adjuvant tamoxifen in premenopausal breast cancer patients. Clin Cancer Res. 2006; 12:4614–4618. [PubMed: 16899609]
51. Zhang JL, Sigmund EE, Rusinek H, et al. Optimization of b-value sampling for diffusion-weighted imaging of the kidney. Magn Reson Med. 2012; 67:89–97. [PubMed: 21702062]
52. Dyvorne HA, Galea N, Nevers T, et al. Diffusion-weighted imaging of the liver with multiple b-values: effect of diffusion gradient polarity and breathing acquisition on image quality and intravoxel incoherent motion parameters–a pilot study. Radiology. 2013; 266:920–929. [PubMed: 23220895]
53. Nilsen LB, Fangberget A, Geier O, Seierstad T. Quantitative analysis of diffusion-weighted magnetic resonance imaging in malignant breast lesions using different b-value combinations. Eur Radiol. 2013; 23:1027–1033. [PubMed: 23111816]
54. Neil JJ, Bretthorst GL. On the use of Bayesian probability theory for analysis of exponential decay data: an example taken from intravoxel incoherent motion experiments. Magn Reson Med. 1993; 29:642–647. [PubMed: 8505900]
55. Barbieri S, Donati OF, Froehlich JM, Thoeny HC. Impact of the calculation algorithm on biexponential fitting of diffusion-weighted MRI in upper abdominal organs. Magn Reson Med. 2015 doi:10.1002/mrm.25765.
56. Orton MR, Collins DJ, Koh DM, Leach MO. Improved intravoxel incoherent motion analysis of diffusion weighted imaging by data driven Bayesian modeling. Magn Reson Med. 2014; 71:411–420. [PubMed: 23408505]

57. Wurnig MC, Donati OF, Ulbrich E, et al. Systematic analysis of the intravoxel incoherent motion threshold separating perfusion and diffusion effects: proposal of a standardized algorithm. Magn Reson Med. 2014 doi:10.1002/mrm.25506.

58. Freiman M, Voss SD, Mulkern RV, Perez-Rossello JM, Callahan MJ, Warfield SK. Reliable assessment of perfusivity and diffusivity from diffusion imaging of the body. Med Image Comput Comput Assist Interv. 2012; 15:1–9. [PubMed: 23285528]

59. Quentin M, Blondin D, Klasen J, et al. Comparison of different mathematical models of diffusion-weighted prostate MR imaging. Magn Reson Imaging. 2012; 30:1468–1474. [PubMed: 22819178]

60. Veraart J, Rajan J, Peeters RR, Leemans A, Sunaert S, Sijbers J. Comprehensive framework for accurate diffusion MRI parameter estimation. Magn Reson Med. 2012 doi:10.1002/mrm.24529:n/a-n/a.

61. Freiman M, Voss SD, Mulkern RV, Perez-Rossello JM, Callahan MJ, Warfield SK. In vivo assessment of optimal b-value range for perfusion-insensitive apparent diffusion coefficient imaging. Med Phys. 2012; 39:4832–4839. [PubMed: 22894409]

62. Freiman M, Perez-Rossello JM, Callahan MJ, et al. Reliable estimation of incoherent motion parametric maps from diffusion-weighted MRI using fusion bootstrap moves. Med Image Anal. 2013; 17:325–336. [PubMed: 23434293]

63. Wu LM, Hu J, Xu JR. MRI in residual tumor size measurement in patient with breast cancer receiving neoadjuvant chemotherapy calls for caution. Breast Cancer Res Treat. 2012; 135:319–320. [PubMed: 22850894]

64. Prevos R, Smidt ML, Tjan-Heijnen VC, et al. Pre-treatment differences and early response monitoring of neoadjuvant chemotherapy in breast cancer patients using magnetic resonance imaging: a systematic review. Eur Radiol. 2012; 22:2607–2616. [PubMed: 22983282]

Key Points

- Novel IVIM biomarkers characterize heterogeneous breast cancer.
- Histogram analysis enables quantification of tumour heterogeneity.
- IVIM biomarkers show relationships with breast cancer malignancy and molecular prognostic factors.

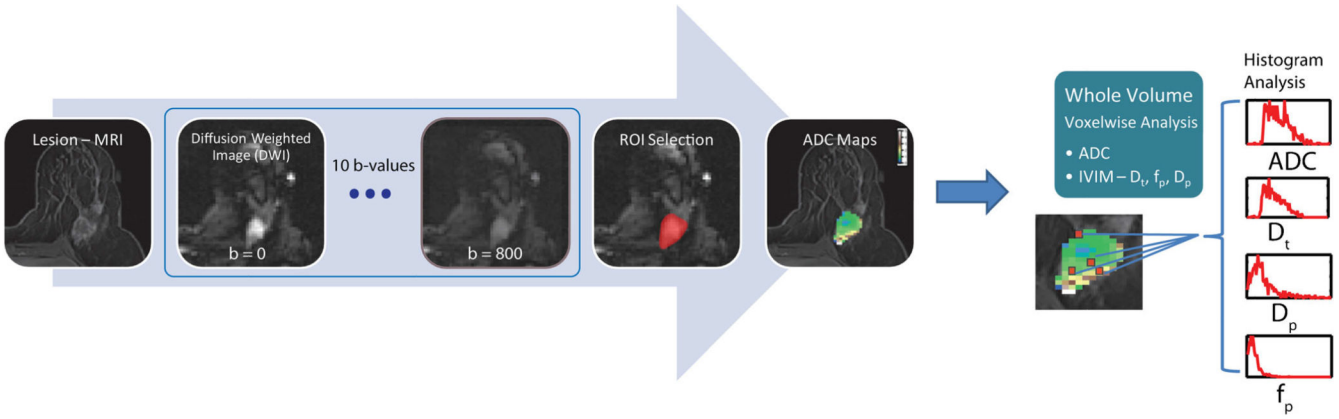

Fig. 1.

General schematic diagram of the DWI and IVIM analyses showing voxel-wise analysis.

Note: The DWI images are from b=0 and 800 s/mm^2

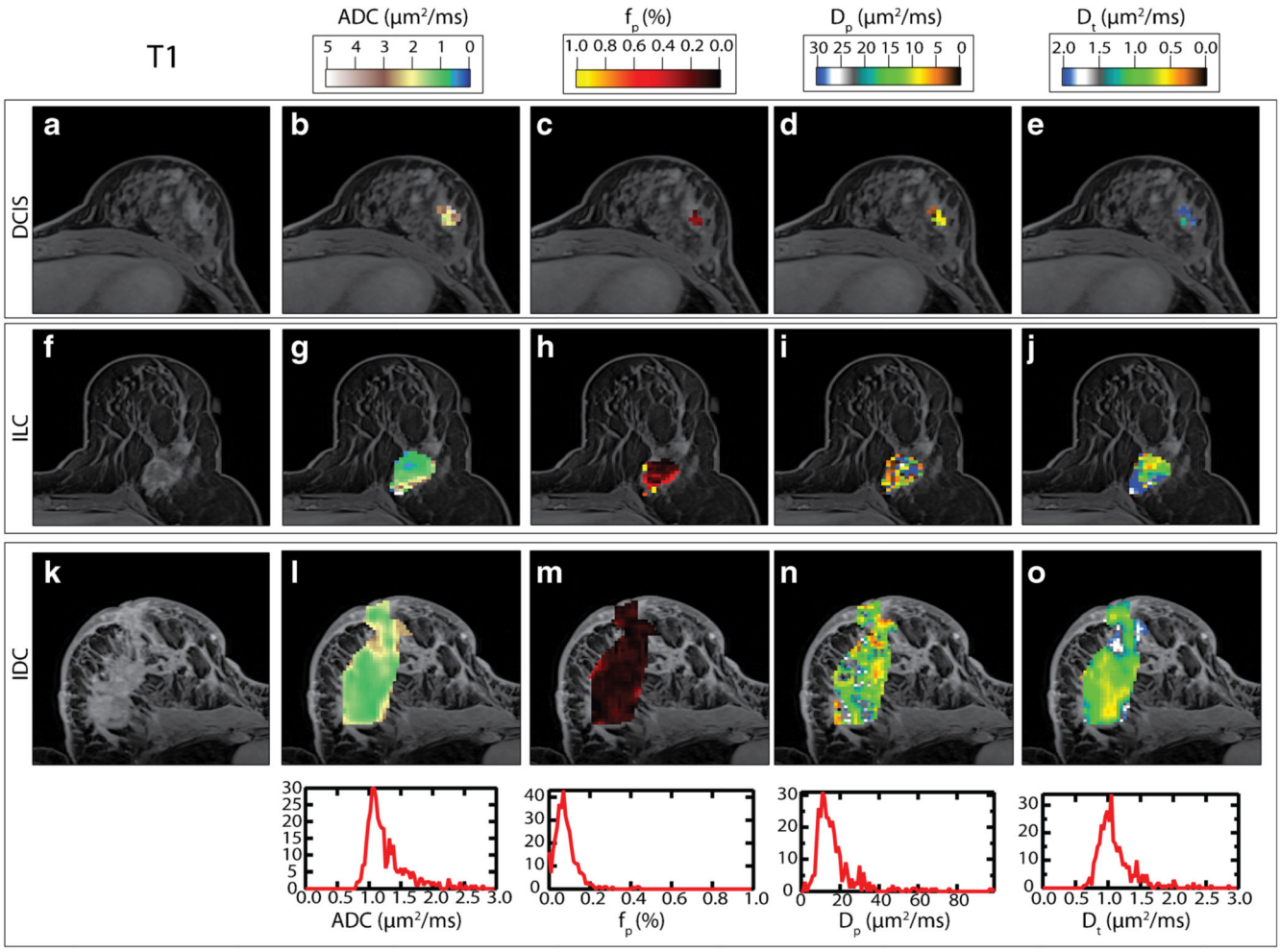

Fig. 2.

ADC and IVIM parameter maps (f_p, D_p, D_t) superimposed on contrast-enhanced T1-weighted MRI within ROIs containing breast tumours. Patient 1 (**a–e**) is a DCIS 53-year-old patient. Patient 2 (**f–j**) is a 59-year-old ILC patient. Patient 3 (**k–o**) is an IDC 62-year-old patient, with the corresponding whole-volume histograms below each of Patient 3's parameter map

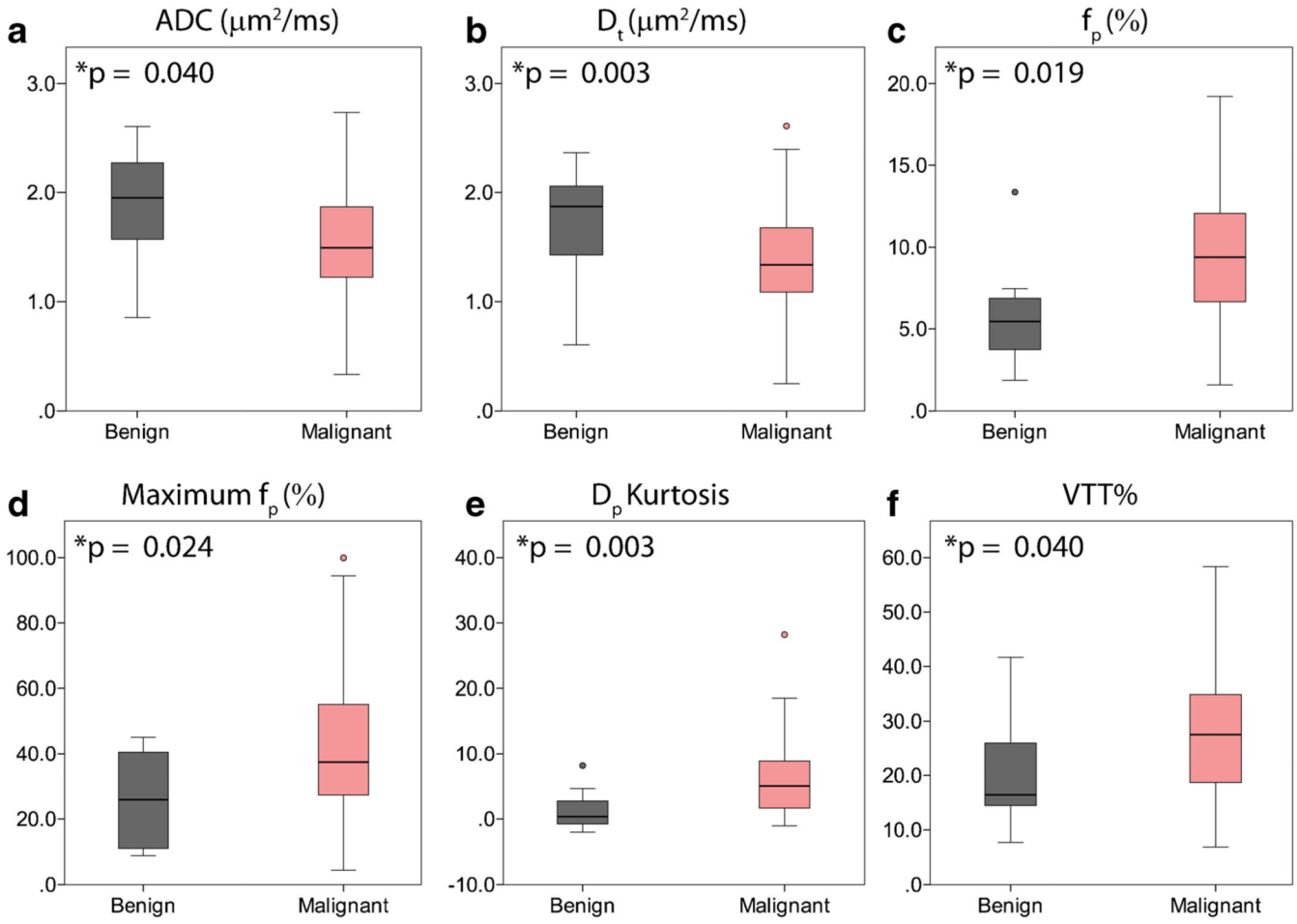

Fig. 3.

Box plot illustration of benign/malignant lesion differentiation from IVIM parameters and histogram analysis. Significant findings ($p<0.05$) are marked with * and their corresponding p value. Refer to Table 2. The *lines* in the box plot indicate the median value and the interquartile range (IQR)

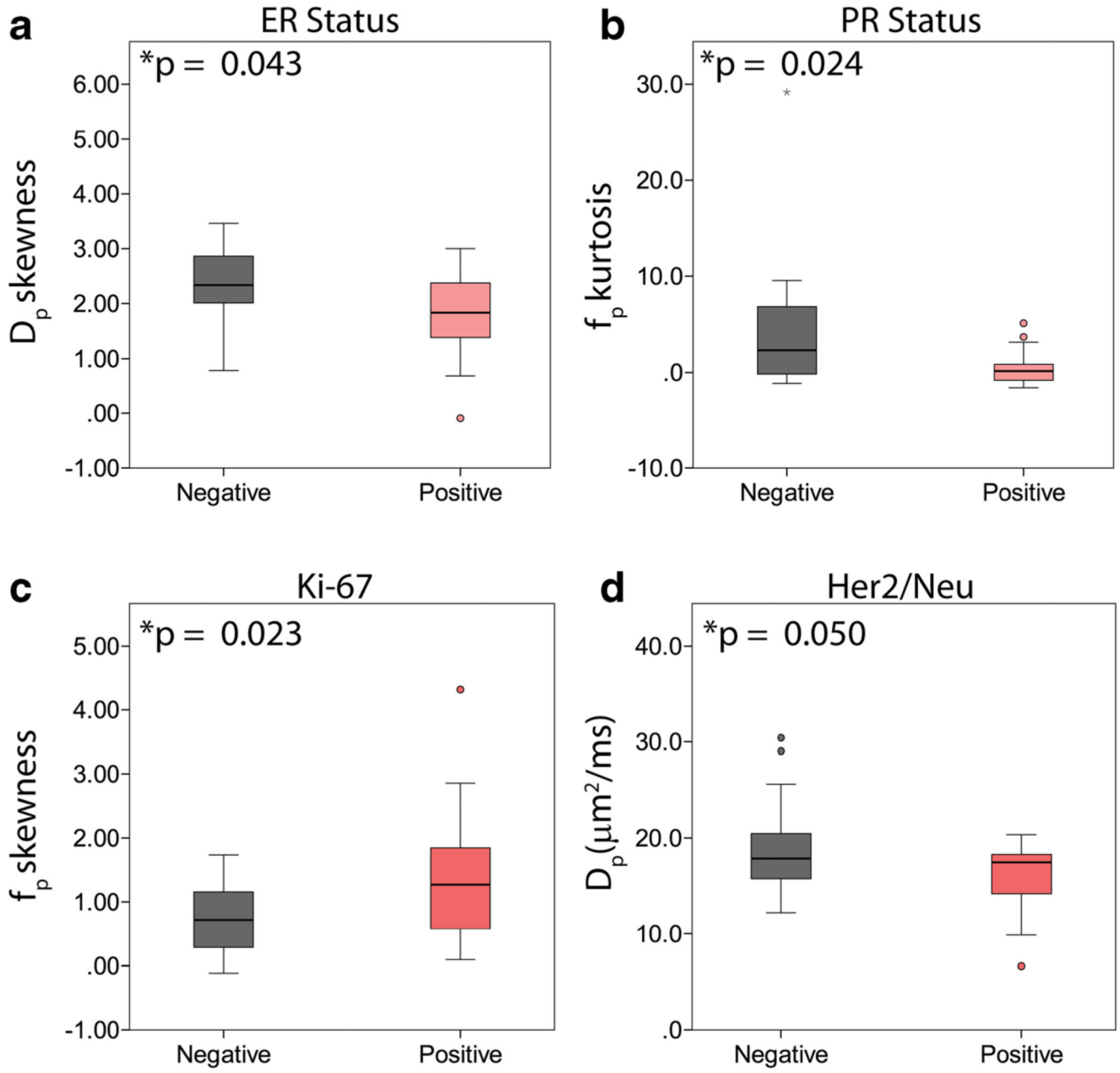

Fig. 4.

Comparison of different vascular IVIM extrema and heterogeneity metrics with hormonal status: (a) ER status vs. D_p skewness, (b) PR status vs. f_p kurtosis, (c) Ki-67 status vs. f_p skewness, and (d) Her2/Neu vs. average value of D_p. All comparisons shown here were significant ($p<0.05$). The *lines* in the box plot indicate the median value and the IQR

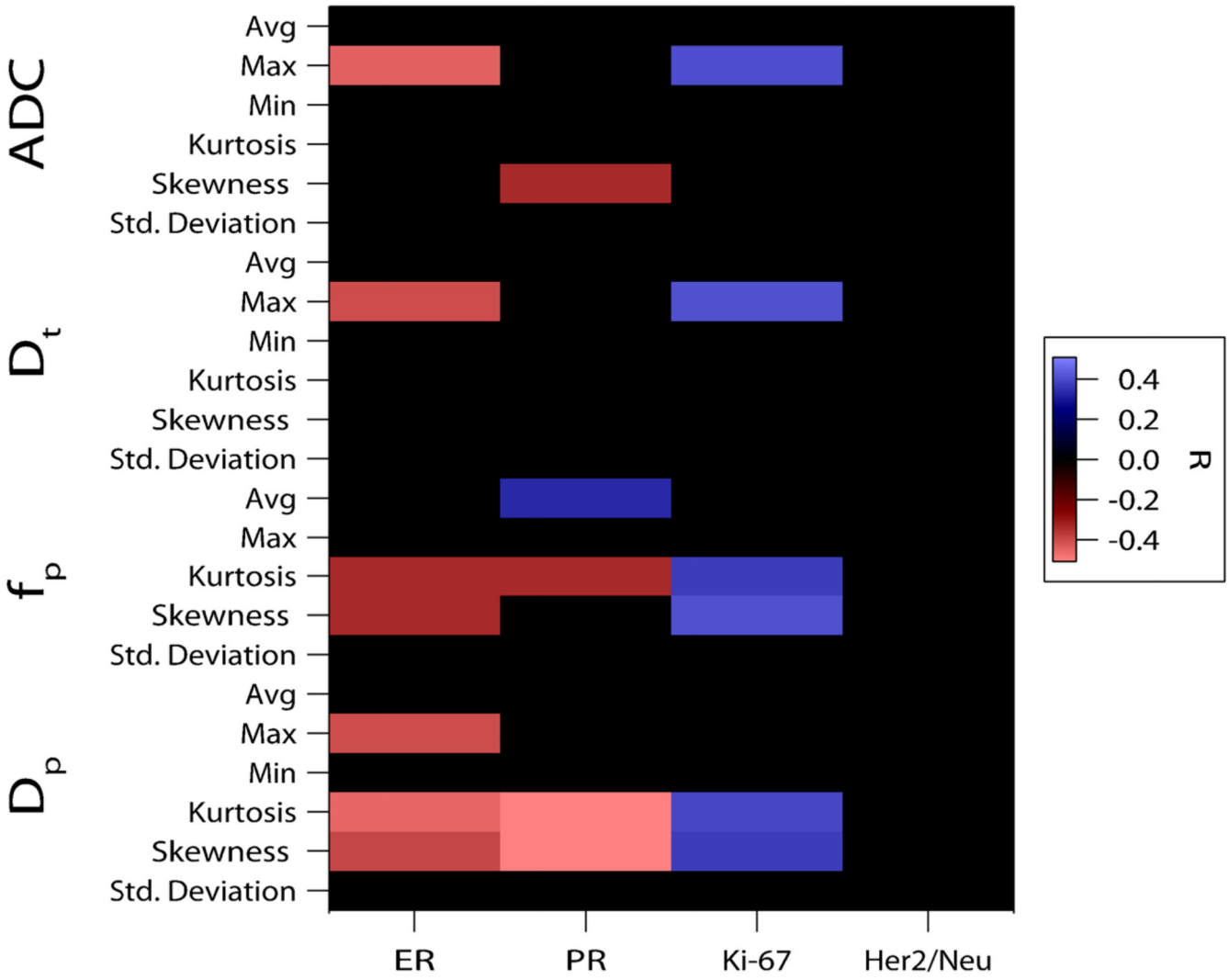

Fig. 5.

Matrix plot of the significant correlation coefficients between IVIM histogram parameters and prognostic factors. *Coloured* entries indicate significant correlations (p<0.05) with positive (*blue*) or negative (*red*) Pearson correlation coefficients R (see *colour scale*)

Table 1

Clinical data for patients enrolled in this study, including benign/malignant status, histological subtype, molecular prognostic status, and treatment paradigm. Note: Certain histological data was not available for each patient

		Number of patients
Benign		**12**
Malignant	Invasive	31
	Mixed	12
	DCIS	7
	Total	**50**
TOTAL		**62**
Molecular prognostic factors		
ER	−	16
	+	29
PR	−	23
	+	22
Ki-67	−	12
	+	25
Her2/neu	−	28
	+	13
Lesion subtyping groups		
ER+HER2−		22
ER+HER2+		7
ER-HER2+		6
ER-HER2− (TN)		15

Table 2

The median and interquartile range (IQR) of each average IVIM value among patients with malignant and benign tumour types. The *p* value results are shown between each mean value comparison along with sensitivity, specificity, and accuracy. Significant differences ($p<0.05$, MW) are marked with an *. Refer to Fig. 3

		Median	IQR	*P* value	AUC	Sensitivity (%)	Specificity (%)	Accuracy (%)
ADC ($\mu m^2/ms$)	Benign	1.82	0.67	0.040*	0.69	58.0	83.3	62.9
	Malignant	1.46	0.68					
D_t ($\mu m^2/ms$)	Benign	1.89	0.70	0.003*	0.77	66.0	91.7	71.0
	Malignant	1.32	0.65					
f_p (%)	Benign	5.0 %	3.0 %	0.019*	0.72	72.0	83.3	72.6
	Malignant	9.1 %	5.1 %					
D_p ($\mu m^2/ms$)	Benign	18.03	16.50	0.10	0.500	100	25.0	85.5
	Malignant	17.73	4.45					

Table 3

The median and IQR of each average IVIM value among patients with different tumour subtypes. The *p* value of each IVIM mean value comparison is shown on the far right column with significant differences ($p<0.05$, MW) marked with an *. † indicates significance using Kruskal–Wallis

	Type	Median	IQR	Comparisons	*P* value
ADC† ($\mu m^2/ms$)	Invasive	1.40	0.42	*Invasive vs mixed*	0.581
	DCIS	2.28	0.57	*Invasive vs DCIS*	**0.008***
	Mixed	1.38	0.55	*Mixed vs DCIS*	**0.025***
D_t † ($\mu m^2/ms$)	Invasive	1.27	0.51	*Invasive vs mixed*	0.884
	DCIS	1.75	0.85	*Invasive vs DCIS*	**0.009***
	Mixed	1.30	0.66	*Mixed vs DCIS*	0.051
f_p (%)	Invasive	9.53	4.21	*Invasive vs mixed*	0.247
	DCIS	7.88	5.15	*Invasive vs DCIS*	0.435
	Mixed	7.46	3.85	*Mixed vs DCIS*	0.966
D_p ($\mu m^2/ms$)	Invasive	17.93	4.02	*Invasive vs mixed*	0.387
	DCIS	19.79	3.85	*Invasive vs DCIS*	0.374
	Mixed	16.30	4.14	*Mixed vs DCIS*	0.225

Table 4

The median, IQR, and *p* value results from extrema and heterogeneity metrics compared with tumour subtypes.

		DCIS (D)		Invasive (I)		Mixed (M)		*P* value	*P* value	*P* value
	Measure	**Median**	**IQR**	**Median**	**IQR**	**Median**	**IQR**	**D vs. I**	**D vs. M**	**I vs. M**
ADC ($\mu m^2/ms$)	Max	2.80	0.36	2.91	0.66	2.35	1.00	0.528	0.058	0.057
	Min	0.91	1.25	0.10	0.71	0.38	0.87	**0.034***	0.295	0.315
	Kurt	0.44	1.45	−0.20	1.64	−0.46	1.09	0.584	0.538	0.527
	Skew†	−0.21	0.73	0.33	0.84	0.22	0.76	**0.026***	0.384	0.066
	SD	0.32	0.13	0.41	0.28	0.31	0.21	0.182	0.833	0.061
D_t ($\mu m^2/ms$)	Max†	2.79	0.39	2.73	0.75	2.14	0.58	0.553	**0.035***	**0.023***
	Min†	0.60	1.05	<0.001	0.54	0.48	0.90	**0.009***	0.189	0.231
	Kurt	−0.29	0.50	−0.033	3.14	−0.48	0.81	0.628	0.595	0.138
	Skew†	−0.086	0.69	0.42	0.93	−0.047	0.87	0.081	0.967	**0.023***
	SD	0.36	0.15	1.27	0.51	0.31	0.11	0.314	0.474	**0.047***
f_p (%)	Max	44.21	5.73	37.14	36.70	27.71	12.41	0.973	**0.035***	0.053
	Kurt	0.98	4.13	0.66	4.86	0.16	3.18	0.420	0.085	0.408
	Skew	1.10	0.68	0.84	0.92	0.72	0.92	0.193	0.067	0.230
	SD	0.058	0.050	8.22	5.70	6.47	2.29	0.743	0.593	0.174
D_p ($\mu m^2/ms$)	Max	97.11	44.48	92.50	23.34	83.81	18.17	0.638	0.488	0.080
	Min	0.072	2.13	<0.001	1.05	0.86	2.01	0.488	0.492	0.054
	Kurt	3.21	2.84	5.58	7.42	4.52	5.83	0.085	0.198	0.475
	Skew	1.77	0.79	2.22	1.23	2.07	1.17	0.115	0.198	0.556
	SD	17.16	3.49	14.18	4.10	14.85	5.56	0.510	0.483	0.567

SD standard deviation

* indicates significant differences ($p<0.05$, MW).

† indicates significance using Kruskal–Wallis

Eur Radiol. Author manuscript; available in PMC 2016 August 01.

Table 5

The median and IQR for average and extremal IVIM values and their *p* value results versus hormonal status. Significant differences ($p < 0.05$, MW) are marked with an *. *SD* standard deviation. *IQR* interquartile range

		Oestrogen receptor							Progesterone receptor				
		Negative		Positive		*p* value			Negative		Positive		*p* value
	Measure	Med.	IQR	Med.	IQR			Measure	Med.	IQR	Med.	IQR	
ADC (μm^2/ms)	Avg.	1.45	0.63	1.45	0.64	0.753	ADC (μm^2/ms)	Avg.	1.43	0.46	1.47	0.83	0.68
	Max.	2.94	0.48	2.56	0.71	**0.025***		Max.	2.92	0.47	2.46	0.80	0.519
	Min.	0.20	0.64	0.47	1.00	0.31		Min.	0.10	0.65	0.59	1.06	**0.047***
	Kurt.	0.04	2.97	−0.27	1.75	0.441		Kurt.	−0.04	2.66	−0.41	1.70	0.141
	Skew.	0.35	1.18	0.12	0.67	0.467		Skew.	0.33	0.76	−0.05	0.73	0.068
	SD	0.46	0.25	0.34	0.20	0.088		SD	0.43	0.28	0.32	0.19	0.052
D_t (μm^2/ms)	Avg.	1.30	0.73	1.31	0.61	0.593	D_t (μm^2/ms)	Avg.	1.21	0.70	1.33	0.67	0.768
	Max.	2.94	0.69	2.26	0.68	**0.018***		Max.	2.85	0.76	2.25	0.70	0.5
	Min.	0.01	0.41	0.34	0.74	0.186		Min.	0.02	0.48	0.39	0.81	**0.050***
	Kurt.	−0.03	3.04	−0.25	1.39	0.9		Kurt.	0.14	3.68	−0.23	0.88	0.19
	Skew.	0.37	1.61	0.26	0.88	0.901		Skew.	0.38	1.46	0.12	0.83	0.161
	SD	0.51	0.30	0.36	0.15	**0.048***		SD	0.51	0.25	0.36	0.18	**0.028***
f_p (%)	Avg.	8.54	4.11	9.16	4.43	0.301	f_p (%)	Avg.	8.53	5.06	9.34	4.05	0.161
	Max.	46.74	37.72	37.15	24.18	0.334		Max.	44.93	41.72	35.72	21.67	0.224
	Kurt.	2.44	8.83	0.40	3.91	0.077		Kurt.	2.32	6.98	0.16	1.74	**0.024***
	Skew.	1.38	1.92	0.97	0.86	0.082		Skew.	1.30	1.44	0.82	0.84	**0.050***
	SD	7.63	7.24	7.17	4.12	0.953		SD	7.28	6.14	7.70	4.62	0.791
D_p	Avg.	17.10	4.21	17.71	6.12	0.656	D_p	Avg.	16.29	4.48	18.53	5.47	0.256
	Max.	92.96	19.17	84.32	31.10	0.063		Max.	92.50	21.90	84.16	38.38	**0.007***
	Min.	0.00	1.13	0.14	1.50	0.246		Min.	0.07	1.23	0.09	1.81	0.164
	Kurt.	7.11	4.91	3.69	5.55	**0.024***		Kurt.	7.00	5.50	2.28	4.22	0.391
	Skew.	2.34	0.90	1.83	1.26	**0.043***		Skew.	2.29	0.84	1.66	1.18	**0.008***
	SD	13.54	3.04	16.20	7.14	0.538		SD	13.59	3.96	16.26	8.39	85

Table 6

(*a*) Significant discrimination of treatment paradigm groups by IVIM histogram parameters by Mann–Whitney group comparisons and by logistic regression. Median values are given with IQR values in parentheses. (*b*) Significant group predictors of prognostic factor status or treatment paradigm. The significance of including each parameter in the combined set along with the combined AUC value for target predication is shown for each target group. *SD* standard deviation

a

Group	Parameter	Mann–Whitney group comparisons			Logistic regression	
		Group Value	Others	p	p	AUC
ER+HER2−	D_p Avg.	19.15 (5.81)	17.47 (3.56)	**0.024***	**0.017***	**0.69**
	D_p Kurt.	2.15 (3.93)	6.14 (5.84)	**0.004***	**0.012***	**0.75**
	D_p Skew.	1.62 (1.10)	2.32 (0.91)	**0.004***	**0.008***	**0.74**
ER+HER2+	ADC Kurt.	−0.56 (0.83)	−0.04 (1.91)	**0.027***	0.059	0.77
	D_p Avg.	15.36 (6.47)	18.19 (4.48)	**0.034***	0.073	0.75
	D_p Kurt.	6.41 (14.05)	4.29 (6.22)	**0.050***	**0.038***	**0.73**
	D_p Skew.	2.38 (2.07)	1.97 (1.28)	**0.023***	**0.017***	**0.76**
TN	D_t Max.	2.97 (0.76)	2.31 (0.71)	**0.004***	0.26	0.70
	f_p Skew.	0.88 (1.98)	1.02 (0.98)	0.16	**0.037***	**0.63**

b

Target	Set of measures			AUC
ER+ or PR+	D_t SD (0.008)	f_p Kurt. (0.0023)	D_p Skew. (0.024)	0.867
	ADC SD (0.025)	f_p Skew. (0.049)	D_p Skew. (0.024)	0.829
PR+	D_tSD (0.018)	f_p Kurt. (0.018)	D_p Skew. (0.026)	0.857
	f_p Skew. (0.023)		D_p Skew. (0.023)	0.783
ER+HER2−	D_p Skew. (0.011)		D_p Avg. (0.026)	0.800